

Mn-Intercalated MoSe₂ under pressure: electronic structure and vibrational characterization of a dilute magnetic semiconductor

Shunda Chen,^{1,2, a)} Virginia L. Johnson,¹ Davide Donadio,^{1, b)} and Kristie J. Koski^{1, c)}

¹⁾*Department of Chemistry, University of California Davis, One Shields Ave. Davis, CA 95616, USA*

²⁾*Department of Civil and Environmental Engineering, George Washington University, Washington, DC, 20052, USA*

(Dated: September 2, 2020)

Intercalation offers a promising way to alter the physical properties of two-dimensional (2D) layered materials. Here we investigate the electronic and vibrational properties of 2D layered MoSe₂ intercalated with atomic manganese at ambient and high pressure up to 7 GPa by Raman scattering and electronic structure calculations. The behavior of optical phonons is studied experimentally with a diamond anvil cell and computationally through density functional theory calculations. Experiment and theory show excellent agreement in optical phonon behavior. The previously Raman inactive A_{2u} mode is activated and enhanced with intercalation and pressure, and a new Raman mode appears upon decompression, indicating a possible onset of a localized structural transition, involving the bonding or trapping of intercalant in 2D layered materials. Density functional theory calculations reveal a shift of Fermi level into the conduction band and spin polarization in Mn_xMoSe₂ that increases at low Mn concentration and low pressure. Our results suggest that intercalation and pressurization of van der Waals materials may allow one to obtain dilute magnetic semiconductors with controllable properties, providing a viable route for the development of new materials for spintronic applications.

^{a)}Electronic mail: shdchen@ucdavis.edu

^{b)}Electronic mail: ddonadio@ucdavis.edu

^{c)}Electronic mail: koski@ucdavis.edu

I. INTRODUCTION

Manganese incorporation in two-dimensional layered and semiconducting materials has received increasing attention as it shows promise for revolutionizing advancements in spintronics¹⁻⁴, nanostructures with ferromagnetic ordering⁵⁻⁷ and tunable functionalities⁷⁻⁹. These perspectives have inspired doping investigations that revealed a plethora of unique magnetic and opto-electronic behaviors. Theory and experiment have shown that Mn doping can lead to ferromagnetic ordering in 2D materials^{6,7,9}. A recent study of the 2D dilute magnetic semiconductor Mn-doped MoS₂ predicts that MoS₂ doped to 10-15% manganese is ferromagnetic at room temperature⁵. Intrinsic ferromagnetism in Mn_xMo_{1-x}S₂ nanosheets, doped by supercritical hydrothermal methods, was reported¹⁰. Mn-doping in MoSe₂ has also been shown to promote additional active sites for hydrogen evolution reactions¹¹. It was also reported that MnBi₂Te₄, an intrinsic magnetic topological insulator, is an ideal platform to realize a high-temperature quantum anomalous hall insulator states¹².

In layered materials, Mn intercalation offers a unique alternative to Mn doping. Intercalation, the insertion of an atom or molecule into the van der Waals gap, provides a chemical handle to tune physical properties including electronic structure and phonon propagation without disturbing the host lattice¹³⁻¹⁵. Intercalation in layered materials has demonstrated an enormous realm of physical and chemical tunability in both current and historical research^{13,15-19}. Through intercalation it is possible to adjust the superconducting temperature^{15,20}, enhance transparency and conductivity²¹⁻²⁴, and reversibly alter optoelectronic behaviors including color and photoluminescence^{22,23,25}. Recently a wet chemical route was achieved to intercalate zero-valent manganese, post-growth, into 2D layered materials¹³, opening a new avenue for experimental study of manganese incorporated two-dimensional materials beyond that of doping.

Molybdenum diselenide (MoSe₂) is a heavily investigated layered n-type indirect band gap semiconductor ($E_g = 1.1$ eV) that shows a transition to a direct band gap with reduction in the number of layers²⁶⁻²⁸. In a recent report, spin states protected from intrinsic electron-phonon coupling were demonstrated in monolayer MoSe₂, reaching 100 ns lifetimes at room temperature²⁹. High-pressure investigations have shown that MoSe₂ does not undergo any phase transitions up to 30 GPa³⁰. Above 40 GPa, a possible semiconductor-metal phase transition has been identified^{31,32}. The effect of Mn intercalation on the pressure-

induced metallization of MoSe₂ is a point of interest, as the intercalated metal may alter the metallization behavior of van der Waals systems³³. Whether pressure favors magnetic ordering at ambient temperature is another point of interest as an analogous mechanism was observed with high concentration of substitutional Mn in monolayer MoS₂⁵. Pressure results in greater wavefunction overlap that could lead to a stronger coupling between isolated Mn intercalant and the MoSe₂ semiconductor electron density, enhancing spin polarization effects. Understanding how structure and bonding in this material system change at pressure can provide crucial insight into its fundamental nature.

Here, through both experiment and first-principles calculations, we show that both the intercalation of manganese into MoSe₂ and pressurization can alter the host structure and its optical phonon frequencies, giving rise to new Raman-active vibrational modes and modifying the electronic band structure. Pressure-dependent Raman scattering, investigated up to 7 GPa under hydrostatic conditions in a diamond anvil cell, suggests the formation of pressure-induced bonding between selenium and the manganese intercalant. First-principles calculations exhibit Raman shifts in agreement with experiments and shed light on the changes of the magnetic and vibrational properties of intercalated MoSe₂ with low Mn content as a function of pressure. In addition, electronic structure calculations provide predictions as for the structural and electronic properties of MoSe₂ intercalated with higher amounts of Mn. Spin-polarized band structure calculations unravel the conditions at which Mn-intercalated MoSe₂ can sustain significant spin currents, making it a suitable dilute magnetic semiconductor.

II. METHODS

A. Manganese Intercalation

Molybdenum diselenide (MoSe₂) was prepared by deposition from as-delivered powder containing large single-crystal platelets onto fused silica substrates followed by drop-casting ethanol onto the substrate to adhere the layered material and prevent loss in solution during intercalation. MoSe₂ single-crystal platelets were on the order of 1–100 μm with varied thicknesses ranging from tens of nanometers to microns.

Zero-valent manganese was intercalated through the decomposition of dimanganese de-

carbonyl ($C_{10}O_{10}Mn_2$) in dilute acetone under inert atmosphere¹³. This route was shown to successfully intercalate manganese into hosts. For completeness, the $MoSe_2$ coated substrates were placed in a 25-50 mL round bottom flask with a reflux condenser attached to a Schlenk line, evacuated, and flushed with N_2 gas. Extra-dry acetone (5 ml) was added to the flask and heated to 48°C. A 10 mM solution of the carbonyl in 5 ml of acetone was added to the flask dropwise over the course of 1.5 hr and kept at 48°C for an additional ~ 1 hr. Substrates were then removed from the solution and rinsed with acetone. All chemicals and powders were obtained from Sigma-Aldrich.

B. High Pressure

High pressures were generated using an Alamax EasyLab mini-Bragg diamond anvil cell (DAC) with Boehler anvils with 0.6 mm culets. Spring steel gaskets were pre-indented to 80-100 μm and drilled with a 250 μm hole. Ruby spheres (Alamax) were used as a pressure calibrant. In the DAC, a solution of 4:1 v/v methanol:ethanol was used as pressure transmitting fluid. Pressures up to 7 GPa were measured to avoid all phase transitions and to remain at relatively hydrostatic pressures of the pressure transmitting fluid. Single crystal platelets were identified optically.

C. Characterization

Raman spectra and ruby fluorescence were measured using a home-built system with a $\lambda = 532$ nm Coherent Sapphire operating with <1 mW on the sample, Leica DMi8 inverted microscope, Princeton Instruments Isoplan SC320, and Princeton Instruments Pixis CCD camera. For Raman spectroscopy, a Semrock laser-edge filter and dichroic with an edge cutoff of ~ 38 cm^{-1} was used with the same apparatus. Acquisition times were on the order of 5 - 15 seconds with 10 - 20 averaged spectra. All spectra were acquired using an 1800 groove/mm grating. Scanning electron microscopy (SEM) and energy dispersive X-ray spectroscopy (EDX) were acquired on 5-10 isolated flakes with a FEI SCIOS Dual-Beam FIB/SEM using an Oxford EDX detector with 10-20 keV accelerating voltage. Transmission electron microscopy (TEM) and selected area electron diffraction (SAED) were acquired using a JEOL 2100Fac operating at 200 keV. X-ray diffraction (XRD) data was acquired

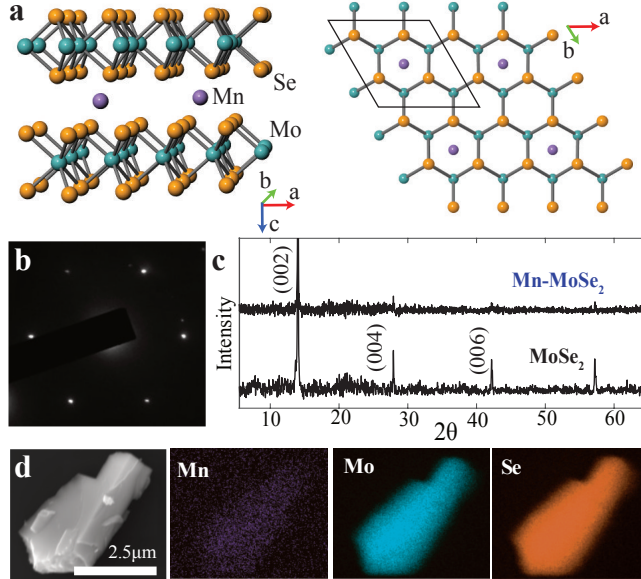


Figure 1. (a) Schematic crystal structure of Mn-MoSe₂. Mn likely occupies octahedral sites. (b) SAED of Mn-MoSe₂ confirms hexagonal structure with intercalation. (c) XRD show expansion of the MoSe₂ host with Mn intercalation. (d) SEM-EDX of Mn-MoSe₂ shows Mn throughout.

using a Bruker D8 Advance Eco with copper k-edge ($\lambda = 1.54 \text{ \AA}$) X-rays. Rietveld refinement was performed with GSAS to determine lattice constants³⁴.

D. First-principles Calculations

Density functional theory (DFT) calculations were performed within the local spin density approximation (LSDA) of the exchange and correlation functional³⁵ by using the Quantum-Espresso package³⁶. Core electrons are treated implicitly through projector augmented wave (PAW) pseudopotentials^{37,38}, and the valence electronic wavefunctions are expanded in a plane-wave basis set with a kinetic energy cutoff of 49 Ry. The charge density is integrated on $16 \times 16 \times 4$ Monkhorst-Pack meshes of k -points for pristine MoSe₂. Structural and cell relaxations are performed using a quasi-Newton optimization algorithm with a convergence criterion of 10^{-4} Ry/Bohr for maximum residual force component. The strong correlation effect of transition metal d-electrons is considered using the LSDA+U method^{39,40}, by introducing a Hubbard type interaction. We use a moderate $U_{eff} = 4$ eV for both Mo and Mn⁴¹⁻⁴⁵. Other U_{eff} values, for example, 2 eV and 6 eV, were tested and consistent results

were obtained. With LSDA+U, the calculated band gap of pure MoSe₂ increases from 0.7 eV to 0.8 eV, with respect to LSDA results. The frequencies of the phonon modes at the Brillouin zone center (Raman shift) as a function of pressure were calculated using density-functional perturbation theory (DFPT)⁴⁶. The threshold for the iterative calculation of the perturbed Kohn-Sham wavefunctions was set to 10⁻¹⁶ Ry. This approach is well suited to predict Raman shift in monolayer and few-layer transition metal dichalcogenides (TMDs) upon strain^{47,48} as well as in bulk⁴⁹.

To model Mn intercalation of MoSe₂ with different Mn concentrations and to account for possible structural changes induced by intercalation, we considered both 2H and 1T' MoSe₂ initial structures⁵⁰, with Mn atom(s) intercalated in the vdW gap (Details are provided in Table S1 in supporting information). The total and spin-polarized carrier concentrations were calculated from DFT spin-polarized Kohn-Sham states integrating the first Brillouin zone on the uniform k-point meshes at least 27 times denser than those k-point meshes used in the self-consistent calculations, using the BoltzTrap software.⁵¹

III. RESULTS AND DISCUSSION

A. Structure and Raman Scattering

The 2H stable phase of MoSe₂ has a hexagonal crystal structure (Figure 1(a); space group: *P6₃/mmc*). The overall host structure is maintained with intercalation as confirmed through SAED (Figure 1(b)) and XRD (Figure 1(c)), which show that also Mn-MoSe₂ is hexagonal. An example SEM image with EDX elemental mapping of Mn-intercalated MoSe₂ (Figure 1(d)) shows that the intercalant is distributed throughout the plates at concentrations of ~1-2 atomic percent (Mn_{0.02}MoSe₂). Nevertheless, XRD would not be suitable to detect local lattice distortions at the intercalation sites.

The intercalation energy per Mn atom, estimated by total energy calculations, depends on Mn concentration, and it is defined as:

$$E_{intercalation} = \frac{E_{Mn_x MoSe_2} - E_{MoSe_2} - n_a E_{Mn}}{n_a} \quad (1)$$

where $E_{Mn_x MoSe_2}$ is the total energy of a MoSe₂ supercell intercalated with an atomic concentration x of Mn, E_{MoSe_2} is the total energy of a 2H-MoSe₂ supercell with the same number of formula units as the intercalated system, E_{Mn} is the energy per atom of bulk *bcc* Mn, and

Table I. Equilibrium lattice parameters of pristine MoSe₂ and Mn-intercalated MoSe₂ from experiments and DFT calculations. In parenthesis it is indicated whether Mn is interstitial within the MoSe₂ layer or in the vdW gap between two layers.

	a Å	c Å	Vol. Å ³
MoSe ₂ (Exp.)	3.285(3)	12.921(3)	120.8(2)
2H-MoSe ₂ (DFT)	3.260	12.718	117.0
Mn _{0.02} MoSe ₂ (Exp.)	3.336(5) (+1.5%)	12.940(5)	124.7(3)
2H-Mn _{0.03} MoSe ₂ (DFT, vdW gap)	3.260	12.801	117.9
2H-Mn _{0.06} MoSe ₂ (DFT, vdW gap)	3.261	12.879	118.6
2H-Mn _{0.125} MoSe ₂ (DFT, vdW gap)	3.261	13.065	120.3
2H-Mn _{0.25} MoSe ₂ (DFT, vdW gap)	3.273	13.423	124.3
1T'-Mn _{0.06} MoSe ₂ (DFT, vdW gap)	3.392	12.227	118.9
1T'-Mn _{0.25} MoSe ₂ (DFT, vdW gap)	3.428	12.021	121.0
1T'-Mn ₁ MoSe ₂ (DFT, vdW gap)	3.501	12.094	124.9
2H-Mn _{0.03} MoSe ₂ (DFT, interstitial)	3.283	12.707	118.6
2H-Mn _{0.06} MoSe ₂ (DFT, interstitial)	3.299	12.710	119.9
2H-Mn _{0.125} MoSe ₂ (DFT, interstitial)	3.353	12.728	123.9

n_a is the number of Mn atoms intercalated. The intercalation energy per Mn atom decreases with increasing Mn concentration, from 2.39 eV/atom with at 3% Mn to 1.96 eV/atom at 25% Mn. This trend and the values are similar to copper and silver intercalation in MoS₂.⁵² Although the intercalation energy per Mn atom decreases slightly with increasing Mn concentration, the total intercalation energy per MoSe₂ unit actually increases as a function of the Mn content from 0.149 eV at 3% Mn to 0.980 eV per unit cell at 25% Mn, indicating that intercalation becomes energetically less favorable the larger the Mn concentration.⁵³

In the hypothetical case of $x = 1$, we find that the most stable phase of Mn₁MoSe₂ would be a 1T' with AA stacking (see Figure S2 in supporting information for the phonon dispersion curves—the absence of the imaginary frequency throughout the Brillouin zone indicates the structural stability), as opposed to the AB stacking of the 2H phase. This intercalation-induced structural transition is analogous to that observed in other metal-intercalated transition metal dichalcogenides, e.g. Li:MoS₂^{54,55}. For $x = 0.25$ the transition

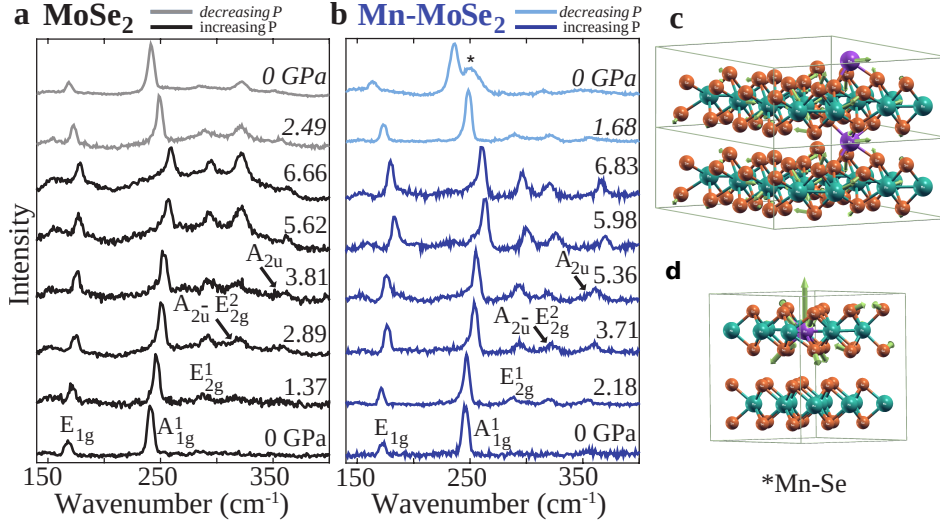


Figure 2. (a) Raman spectra under pressure of pristine MoSe₂ and (b) Mn-intercalated MoSe₂ (black and dark blue lines for increasing pressure, gray and cyan lines for decreasing pressure). The asterisk, described in the text, coincides with the Raman frequency of a Mn-Se bond. (c) Force vectors for the mode at $\sim 250 \text{ cm}^{-1}$ in 1T'-Mn_{0.06}MoSe₂ from DFT calculations, showing a collective optical mode that involves displacements of Mn, Mo and Se atoms, possibly corresponding to the * Mn-Se peak in experiment. (d) Force vectors for the Mn-Se collective mode at $\sim 250 \text{ cm}^{-1}$ in 2H-Mn_{0.06}MoSe₂ with Mn at interstitial site from DFT calculations, which might also correspond to the * Mn-Se peak in experiment.

to 1T' lowers the total energy by 0.178 eV per MoSe₂ formula unit. Conversely, at lower Mn concentration, for example $x=0.125$, the 2H phase has lower energy than the 1T' phase by 0.103 eV per MoSe₂ formula unit (formation energies per MoSe₂ formula unit are summarized in Table S1 in supporting information). These calculations predict the 1T' phase to be stable at higher Mn concentration ($x \geq 0.25$), and the 2H phase to remain stable at low Mn concentration ($x \leq 0.125$). At ambient condition the system would then stay in the 2H phase upon intercalation at the low Mn concentrations of the experiment.

Successful intercalation of manganese is confirmed by XRD, which shows an expansion of the host lattice constants and the unit cell volume (Table I; Figure 1(c)). This expansion is associated with insertion of atoms into the van der Waals gap^{13,56}. Expansion of the unit cell volume is measurable, with an almost 3% increase even at low Mn concentrations. The volume change calculated using DFT is similar with $\sim 1\text{-}6\%$ expansion, depending upon the Mn intercalation concentration. Experiments with very low Mn concentration show a mild

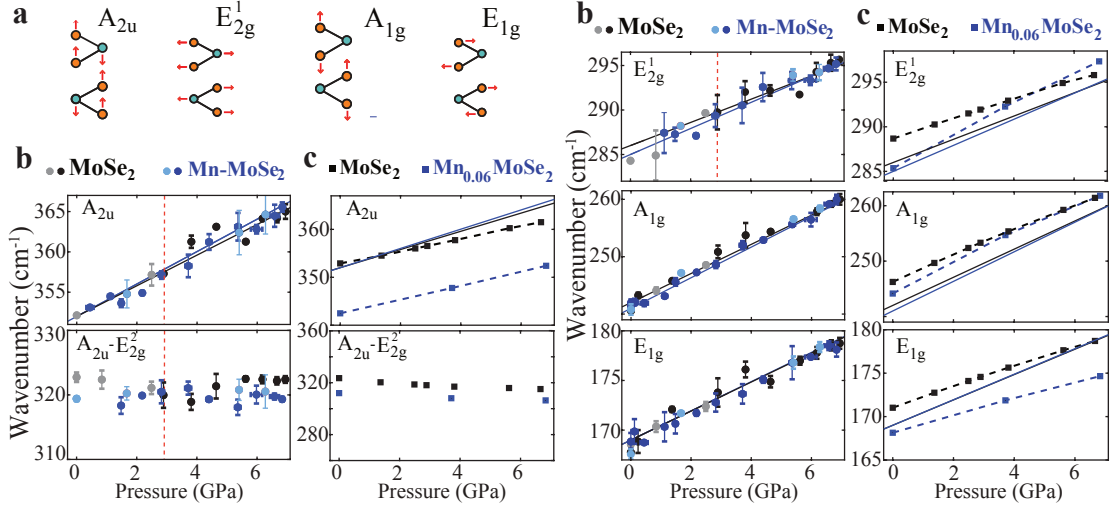


Figure 3. (a) Mode schematics. (b) Experimentally determined Raman shifts for pristine MoSe_2 and $\text{Mn}_{0.02}\text{MoSe}_2$ under pressure (black and dark blue full circles for increasing pressure, gray and cyan full circles for decreasing pressure). For pristine MoSe_2 , A_{2u} , $A_{2u}-E_{2g}^2$, and E_{2g}^1 modes appear after 2.89 GPa as indicated with a red vertical dashed line. (c) DFT calculated Raman shifts for pristine MoSe_2 and $\text{Mn}_{0.06}\text{MoSe}_2$. The linear fit of the experimental shifts are solid lines for reference.

~ 0.05 Å expansion of the in-plane lattice parameter (a) upon intercalation and a ~ 0.02 Å expansion of the cross-plane lattice parameter (c). DFT calculations for low concentrations of Mn in the 2H phase would predict an expansion of the c -axis only, while a expands at higher concentration of Mn. In contrast, if intercalation is accompanied by a transition to the 1T' structure, a expands and c contracts. While a complete transition to 1T' cannot occur at such low Mn concentration, we argue that the a expansion observed in experiments stems from local distortions around the intercalation sites, which also disrupt the long range crystalline order of the system, as suggested by the disappearance of the high order peaks in XRD (Figure 1(c)).

Raman spectra of MoSe_2 and Mn-MoSe_2 as a function of pressure are presented in Figure 2. The observed in-plane modes are E_{2g}^1 at 168 cm^{-1} and E_{2g}^2 at 286 cm^{-1} . The only Raman active out-of-plane mode is the A_{1g} mode, which is initially at 242 cm^{-1} ³⁰. A peak at 354 cm^{-1} is seen at pressures above 2.89 GPa and can be assigned as A_{2u} ²⁶. It is an infrared active phonon that is forbidden in Raman scattering⁵⁷, as confirmed by DFT calculations. Previous studies observe this peak at higher excitation energies at ambient

conditions and reason that resonance effects allow this peak to be observable^{26,58}. This mode has also been observed at higher pressures^{31,32}. Intercalation of manganese and application of pressure may result in symmetry breaking allowing the forbidden mode to appear in Raman spectra. Symmetry breaking may also be responsible for the appearance of the E_{2g}^1 mode at higher pressures. With increasing pressure, both modes increase in scattering intensity³⁰⁻³². Symmetry breaking with pressure is common and not unexpected. These additional peaks may have been observed in these high pressure studies over other investigations because of the high resolution grating used.

An additional feature not observed in MoSe_2 appears post decompression at approximately 250 cm^{-1} in Mn-MoSe_2 (labeled * in Figure 2(a)). The frequency of this mode matches a calculated longitudinal optical phonon mode in wurtzite MnSe , suggesting bonding between the Mn intercalant and the host with released pressure.⁵⁹ Through DFT calculations we found that this mode is related to the formation of a bond between the host structure and the intercalant guest. This may, however, happen in different ways: either through a transition to the metastable $1T'$ structure or through the interstitial embedding of Mn into a MoSe_2 layer, which was recently proposed in MoSe_2 monolayer on the basis of DFT calculations.⁶⁰

In fact, the 250 cm^{-1} peak appears in the calculation of $1T'$ Mn-intercalated MoSe_2 at any given concentration of intercalant from 0.06 to 0.25. The frequency corresponds to a collective optical mode that involves displacements of both Mn, Mo and Se atoms (Figure 2(c) and Figures S3-S4). Since Mn atoms into interstitial sites might be another possible explanation for the onset of the new mode observed in experiment, we computed the phonon frequencies of Mn-MoSe_2 with Mn at the interstitial site at 12.5%, 6% and 3% Mn concentrations. With Mn at the interstitial site, the calculated in-plane lattice expansion rates are 2.9%, 1.2% and 0.7% for Mn concentrations at 12.5%, 6% and 3%, respectively (see Table I for the optimized lattice parameters). The calculated in-plane expansion rates for Mn at interstitial are in good agreement with the in-plane lattice expansion rate 1.5% measured in experiment at low Mn concentration of 1-2%. However, the frequency of the Mn-Se collective mode is sensitive to the Mn concentration. At 12.5% of Mn, the calculated Mn-Se collective mode appears at $\sim 240 \text{ cm}^{-1}$ (see Figure S7), which is lower than new mode observed at 250 cm^{-1} in the experiment. And at 6% Mn concentration, the calculated Mn-Se collective mode appears at around 250 cm^{-1} , in very good agreement with

the measured value (see Figure 2(d) and Figure S8). But at 3% Mn concentration, the Mn-Se collective vibrational mode blue-shifts to around 256 cm^{-1} (see Figure S9 in supporting information). Given the linear shift of the frequency of Mn-Se mode with Mn concentration, one could not conclude that the new mode at 250 cm^{-1} observed in experiment is solely due to the interstitial trapping of Mn. Since the 250 cm^{-1} peak appears in the calculation of $1T'$ Mn-intercalated MoSe_2 at any given concentration, we would conjecture that both (i) Mn bound in the vdW gap and (ii) Mn bound in interstitials are possible. However, it remains open whether Mn binds more in the vdW gap or in interstitials and there is no simple experimental route to directly address this hypothesis. These results suggest that Mn intercalation combined with compression and decompression processes may provide possible new routes to Mn interstitial doping of layered materials.^{60,61}

Figure 3 shows the measured (Figure 3(b)) and calculated (Figure 3(c)) vibrational frequencies for each Raman mode as a function of pressure. Figure 3(a) shows the schematic of each vibrational mode. In Figure 3(c), calculated Raman shifts are plotted alongside the linear fit of the experimental shifts in solid black and blue line for MoSe_2 and Mn- MoSe_2 , respectively. DFT calculated Raman shifts are in very good agreement with experimental results. Though experimental data do not show significant Raman shifts upon Mn intercalation with low concentrations of Mn intercalant of $\sim 1\text{-}2$ atomic %, DFT calculations suggest that the frequency of the Raman shift would decrease with higher Mn concentration at ambient and relatively low pressure (please see Figure 3, and Figure S1 in supporting information).

Table II provides the initial Raman frequency, ω_0 , at ambient pressure and the change in frequency with pressure ($\frac{d\omega}{dP}$). Despite a detectable change in the host unit cell volume (Table I), with low concentrations of Mn intercalant of $\sim 1\text{-}2$ atomic %, the experimentally measured Raman frequency shift of each mode in MoSe_2 does not change significantly upon Mn intercalation (Table II). This is not unusual. Experimentally, shifts of the Raman modes with intercalation are complex⁶². Optical phonons can exhibit stiffening, softening, or no change with intercalation affected by the acceptor or donor nature of the intercalant as well as the associated change in the host volume with intercalation⁶².

From the experimental data, the frequency of the Raman shift of each mode tends to

Table II. Ambient pressure Raman frequencies (cm^{-1}), Raman shift pressure-derivative, $\frac{d\omega}{dP}$ ($\frac{cm^{-1}}{GPa}$), and isothermal mode Grüneisen (γ_T) for observed modes calculated from Equation (2).

	E_{1g}			A_{1g}^1		
	ω_o (cm^{-1})	$\frac{d\omega}{dP}$ ($\frac{cm^{-1}}{GPa}$)	γ_T	ω_o (cm^{-1})	$\frac{d\omega}{dP}$ ($\frac{cm^{-1}}{GPa}$)	γ_T
MoSe ₂ (Exp.)	167.8(6)	1.68(8)	0.46(2)	240.6(6)	2.9(1)	0.54(2)
MoSe ₂ (DFT)	171.02	1.15(2)	0.307(5)	246.24	2.24(4)	0.416(7)
Mn _{0.02} MoSe ₂ (Exp.)	167.6(6)	1.67(6)	0.46(2)	241.3(6)	2.67(4)	0.506(8)
Mn _{0.06} MoSe ₂ (DFT)	168.20	0.96(7)	0.261(2)	244.44	2.6(4)	0.486(3)
Mn _{0.125} MoSe ₂ (DFT)	165.52	0.90(3)	0.248(8)	241.45	1.88(5)	0.55(1)
Mn _{0.25} MoSe ₂ (DFT)	158.16	0.5(2)	0.144(1)	207.21	2.1(2)	0.463(3)
	E_{2g}^1			A_{2u}		
	ω_o (cm^{-1})	$\frac{d\omega}{dP}$ ($\frac{cm^{-1}}{GPa}$)	γ_T	ω_o (cm^{-1})	$\frac{d\omega}{dP}$ ($\frac{cm^{-1}}{GPa}$)	γ_T
MoSe ₂ (Exp.)	286(1)	1.3(2)	0.21(3)	354.2(2)	1.5(4)	0.20(5)
MoSe ₂ (DFT)	289	1.08	0.171(1)	352.8	1.31	0.215(1)
Mn _{0.02} MoSe ₂ (Exp.)	285.2(5)	1.5(1)	0.23(2)	351.5(5)	2.0(1)	0.26(1)
Mn _{0.06} MoSe ₂ (DFT)	285.48	1.8(1)	0.288(2)	342.45	1.45(3)	0.194(1)
Mn _{0.125} MoSe ₂ (DFT)	279	1.29	0.240(2)	331	0.899	0.1200(8)
Mn _{0.25} MoSe ₂ (DFT)	269.76	1.4(2)	0.237(2)	316.01	0.1(4)	0.0145(1)

decrease slightly, except the A_{1g} mode. Though the frequency of the Raman shift of the A_{1g} mode seems to increase by about $0.7 cm^{-1}$ (Table II), the measurement error is comparable to the size of the change. From DFT calculations, with higher Mn concentration, it looks more likely that the frequency of the Raman shift of each mode would decrease upon Mn intercalation at ambient and relatively low pressure (see Figure 3 and Figure S1 in supporting information). The experimental Raman shift of Mn-MoSe₂ and MoSe₂ modes show very similar linear pressure-dependent slope ($\frac{d\omega}{dP}$) (Figure 3, Table II). For pristine MoSe₂, the E_{2g}^1 and A_{2u} modes do not show up until pressure of ~ 2.89 GPa and remain with decompression^{57,63}. An anomalous mode shows up around $320 cm^{-1}$. DFT calculations suggest this might be ascribed to the A_{2u} - E_{2g}^2 combination band. This mode does not appear in MoSe₂ until about ~ 2.89 GPa, as indicated by a dashed red line in Figure 3.

This mode persists with decreasing pressure, which is consistent with the appearance of the A_{2u} mode. It occurs in Mn-MoSe₂ at around ~ 1 GPa. This peak shows no change with pressure as Raman shifts of both the E_{2g}^2 and the A_{2u} increase. Thus, there is no significant pressure-derivative of this mode. All modes show phonon stiffening, increasing linearly with pressure, except the overtone mode A_{2u} - E_{2g}^2 at around 320 cm^{-1} as discussed above.

Compressibility of MoSe₂ and MnMoSe₂ can be described using the isothermal mode Grüneisen parameter (γ_T):

$$\gamma_T = - \left(\frac{d \ln \omega}{d \ln V} \right)_T = \frac{B_T}{\omega_0} \left(\frac{d\omega}{dP} \right)_T \quad (2)$$

where B_T is the isothermal bulk modulus. Using the third-order Birch-Murnaghan equation of state to fit *in situ* high-pressure MoSe₂ X-ray diffraction data, Aksoy⁶⁴ *et al.* calculated B_T as 45.7 ± 0.3 GPa. DFT calculations here find a bulk modulus of 47.9 GPa for MoSe₂, close to experiments⁶⁴, and 51.3 GPa for Mn_{0.125}MoSe₂. Mn-intercalation should yield a notable decrease in the isothermal compressibility. With pressure, the empty van der Waals gap should compress first. By adding more atoms to the gap, Mn-intercalation subsumes space otherwise available for compression. Thus, intercalation makes the material less compressible. Using these values of B_T , along with the relevant values of ω_0 and $\frac{d\omega}{dP}$, the mode Grüneisen is calculated from Equation 2 for all modes (Table II). Calculated isothermal mode Grüneisen parameters in most cases exhibit similar trends as experiments, however with large uncertainties, mostly due to shortcoming related to the approximated density functional. However, the overall agreement between Raman measurements and DFT calculations suggests that the adopted level of theory accounts well for the charge redistribution upon intercalation, and DFT calculations can be used to predict the electronic structure of Mn-intercalated MoSe₂.

B. Electronic Band Structure

Figure 4 shows the electronic band structures of pristine MoSe₂, Mn_{0.03}MoSe₂ and Mn_{0.125}MoSe₂ at 0 GPa and ~ 7 GPa. For pristine MoSe₂, with the increase of pressure, the band gap narrows from 0.8 eV at 0 GPa to 0.4 eV at 6.66 GPa (Figure 4(d)). Upon intercalation of Mn, the overall host structure is retained (Figure 4(b) and (c)). At higher concentrations of Mn intercalant (Mn_{0.125}MoSe₂, Figure 4(c)) the Fermi level lies deeper in

the conduction band. While pressure tends to close the gap between the valence and the conduction band also in intercalated systems, the position of the Fermi level and the carriers concentration are determined by doping and do not change significantly upon compression (Figure 5(a)). The transition to the 1T' phase would lead to the metallization of the system, with substantial change of the band structures and spin-polarized density of states. (See Figure S5 in supporting information for the spin-polarized electronic band structure for 1T' phase Mn-intercalated MoSe₂.) Conversely, when Mn gets trapped in the interstitial of the MoSe₂ layer, the system remains semiconducting with a localized spin state in the gap, below the Fermi level (Figure S10).

The calculated projected density of states (PDOS) are shown in Figure 4 for pristine and Mn-intercalated MoSe₂ at 0 GPa and at ~ 7 GPa. Mn intercalation in MoSe₂ shows clear signatures of spin polarization. At low concentrations of Mn (Mn_{0.03}MoSe₂), there is clear separation of the density of spin-up and spin-down electrons which suggest spin polarized current is possible in Mn-intercalated MoSe₂. With pressure, the spin separation between the spin-up and spin-down states is reduced. At 0 GPa the overall magnetic moment of the Mn_{0.03}MoSe₂ and Mn_{0.125}MoSe₂ supercell is 5.00 μ_B . With pressure (at 6.83 GPa), the overall magnetic moments reduce slightly to 4.61 μ_B and 4.54 μ_B for Mn_{0.03}MoSe₂ and Mn_{0.125}MoSe₂, respectively.

The calculated total (n-type) carrier concentrations increase with increasing Mn, proportional to Mn concentration, and do not shift significantly with pressure (Figure 5(a)). 2D semiconductors with dilute magnetic manganese impurities should have conduction completely ruled by spin polarization^{1,5}. One would expect that with increasing manganese concentration and increasing pressure, the concentration of spin-polarized carriers would also change with competing effects due to spin overlap. The spin interaction should increase as the manganese concentration increases (Figure 4(c)), thus decreasing the spin-polarized carrier concentration. As pressure is increased, one would expect a similar effect, as the spin overlap and spin interaction also increase. Calculations of the spin-polarized carrier concentration as a function of pressure and manganese concentration (Figure 5(b)) reveal that the concentration of net spin-polarized carriers depends on both pressure and Mn concentration. Small concentrations of Mn show the greatest amount of spin-polarized carriers, with 3 atomic % (close to that achieved by experiment) as a maximum. It is interesting that at low concentration of Mn (3%), pressure reduces the spin-polarized carrier concentration, while at

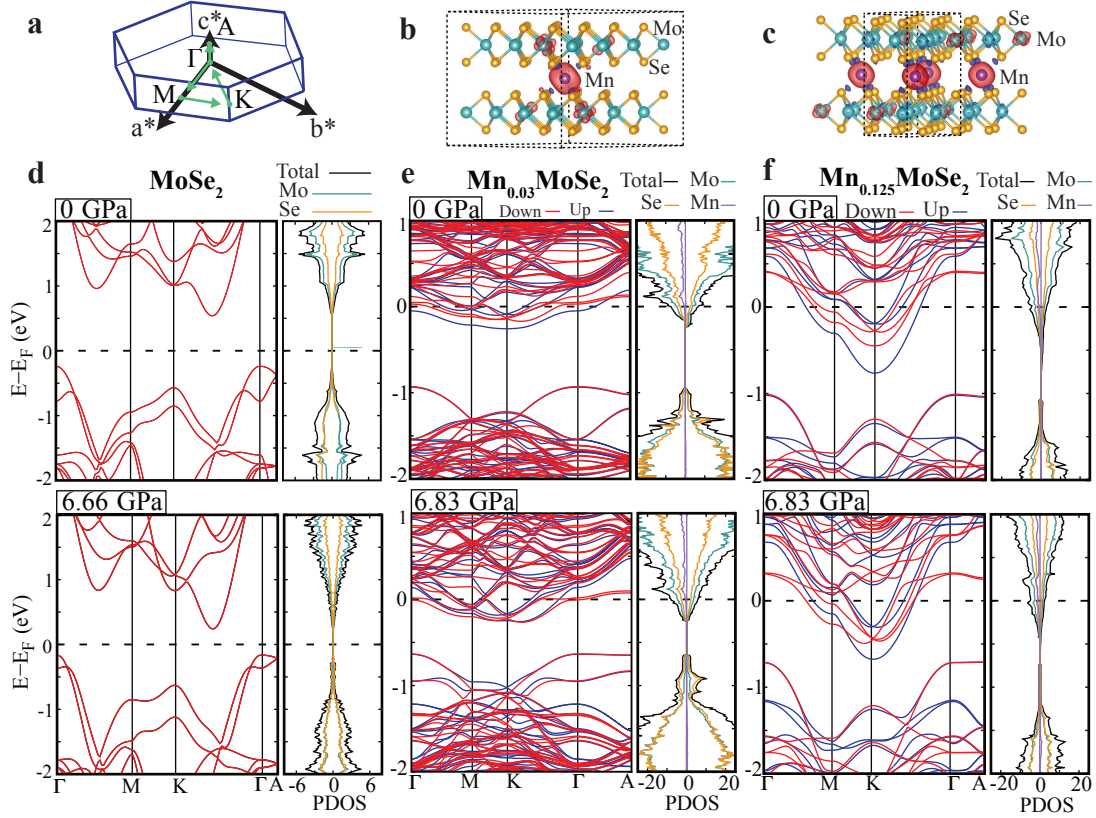


Figure 4. (a) Brillouin zone schematic of MoSe_2 . (b) $\text{Mn}_{0.03}\text{MoSe}_2$ structure and (c) $\text{Mn}_{0.125}\text{MoSe}_2$ structure at 0 GPa with spin density and polarization; red and blue isosurfaces represent positive and negative spin density, respectively. (d) Electronic band structure of MoSe_2 at 0 GPa (above) and 6.66 GPa (below). Projected density of states are given for either pressure to the right of the band structure. The band structure and PDOS of (e) $\text{Mn}_{0.03}\text{MoSe}_2$ and (f) $\text{Mn}_{0.125}\text{MoSe}_2$ show that Mn intercalation metallizes the material moving the Fermi level into the conduction band. Manganese states are spin polarized in the conduction band and the population of states increases with pressure as the band gap narrows.

higher concentration (above approximately 6%), pressure increases the spin-polarized carrier concentration (Figure 5(b)). The local structural transition, suggested by the appearance of the 250 cm^{-1} peak in the Raman spectrum upon decompression, would substantially affect the electronic structure of the intercalated material and spin separation. (See Figure S5 for the band structure and spin-polarized density of states of $1\text{T}'$ phase of Mn-intercalated MoSe_2 , and Figure S6 for the spin-polarized carrier concentration. It's interesting that both 2H and $1\text{T}'$ phases show similar trends in spin polarization as a function of Mn concentra-

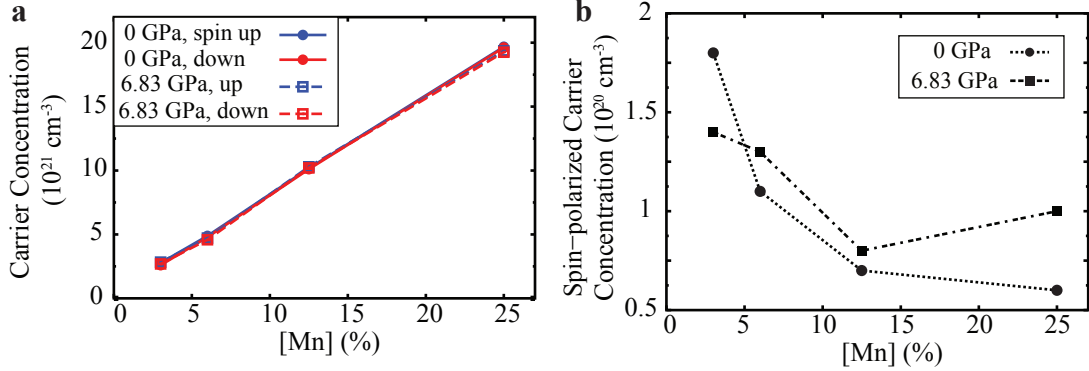


Figure 5. (a) Spin up and spin down carrier concentration as a function of Mn concentration at 0 GPa and 6.83 GPa. (b) Total spin-polarized carrier concentration (the difference between spin up and spin down carrier concentrations).

tion, and the spin-polarized carrier concentration for 1T' phase of Mn-intercalated MoSe₂ could reach up to $\sim 1 \cdot 10^{20} \text{ cm}^{-3}$ at around 11% of Mn concentration.) These competing effects reveal the chemical and thermodynamic tunability of MoSe₂ spin-polarized carriers. The predicted concentration of spin polarized carriers, up to $\sim 2 \cdot 10^{20} \text{ cm}^{-3}$ in 2H phase and $\sim 1 \cdot 10^{20} \text{ cm}^{-3}$ in 1T' phase, could possibly be observed by Hall measurements and is significantly high to enable spintronic applications.

IV. CONCLUSIONS

This work illustrates the ability to adjust the phonon frequencies and the electronic band structure with Mn intercalation and pressure. The appearance of a new phase is found associated with Mn guest bonding with the host MoSe₂. These results suggest intercalation systems under high pressure can lead to unique bonding environments and, thus, new materials. These findings set precedent for further investigation into Mn-intercalation of 2D layered materials as an alternative to dilute magnetic doping. The robustness of this system is demonstrated by both intercalated and non-intercalated pressure-dependent phonon frequencies. DFT calculations show that Mn-intercalation causes the Fermi level to shift into the conduction band, rendering the system an n-type semiconductor or nearly metallic. Manganese intercalated MoSe₂ retains a total magnetic moment that corresponds to that of single Mn atoms. Unpaired spins contribute to the density of states near the Fermi level,

thus potentially enabling spin currents. Pressure reduces the spin carrier density at low Mn concentration, but it slightly increases it at higher Mn concentration. The spin polarized behavior predicted in intercalated Mn-MoSe₂ here has the potential to surpass that of doped systems, with the advantage that transition metal atoms may be intercalated post-growth. These results provide insights into how concentration limitations in dilute manganese doped MoSe₂ may be bypassed by exploiting the van der Waals gap of a layered material through intercalation and high pressure. We expect that resistivity studies as a function of pressure and magnetic field may further elucidate the nature of Mn spin-polarized carriers in this host.

SUPPLEMENTARY MATERIAL

DFT calculated Raman shifts with higher Mn concentrations shown as a function of pressure and Mn concentration, in comparison with experimentally determined Raman shifts; detailed information for constructing Mn-intercalated MoSe₂ structures for DFT calculations with various Mn concentrations in 2H and 1T' phases with Mn in vdW gap, as well as 2H phase with Mn at interstitial site of MoSe₂, and the corresponding Monkhorst-Pack k -point meshes and formation energy; phonon dispersion curves for 1T'-Mn₁MoSe₂; force vectors of the mode at $\sim 250 \text{ cm}^{-1}$ in 1T'-Mn_{0.06}MoSe₂ and 1T'-Mn_{0.25}MoSe₂; spin-polarized electronic band structure and PDOS of the 1T' phase of Mn-intercalated MoSe₂ at 0 GPa; total spin-polarized carrier concentration for 1T' phase of Mn-intercalated MoSe₂ as a function of Mn concentration at 0 GPa and 6.83 GPa; force vectors of the Mn-Se collective mode in 2H-Mn_{0.125}MoSe₂, 2H-Mn_{0.06}MoSe₂ and 2H-Mn_{0.03}MoSe₂ with Mn at interstitial site of MoSe₂; spin-polarized electronic band structure and PDOS of 2H-Mn_{0.03}MoSe₂ with Mn at interstitial site of MoSe₂.

DATA AVAILABILITY

The data that support the findings of this study are available from the corresponding author upon reasonable request.

ACKNOWLEDGMENTS

We thank Bryan P. Moser and Daniel R. Williams for XRD patterns and SEM images, respectively. This work was supported by the Office of Naval Research (N00014-16-1-3161).

REFERENCES

- ¹K. Sato, L. Bergqvist, J. Kudrnovsky, P. H. Dederichs, O. Eriksson, I. Turek, B. Sanyal, G. Bouzerar, H. Katayama-Yoshida, V. A. Dinh, T. Fukushima, H. Kizaki, and R. Zeller, “First-principles theory of dilute magnetic semiconductors,” *Rev. Mod. Phys.* **82**, 1633 (2010).
- ²T. Dietl, “A ten-year perspective on dilute magnetic semiconductors and oxides,” *Nature materials* **9**, 965 (2010).
- ³H. Ohno, “A window on the future of spintronics,” *Nature Materials* **9**, 952–954 (2010).
- ⁴T. Dietl and H. Ohno, “Dilute ferromagnetic semiconductors: Physics and spintronic structures,” *Reviews of Modern Physics* **86**, 187–251 (2014).
- ⁵A. Ramasubramaniam and D. Naveh, “Mn-doped monolayer MoS₂: an atomically thin dilute magnetic semiconductor,” *Phys. Rev. B* **87**, 195201 (2013).
- ⁶R. Mishra, W. Zhou, S. J. Pennycook, S. T. Pantelides, and J.-C. Idrobo, “Long-range ferromagnetic ordering in manganese-doped two-dimensional dichalcogenides,” *Phys. Rev. B* **88**, 144409 (2013).
- ⁷J. Wang, F. Sun, S. Yang, Y. Li, C. Zhao, M. Xu, Y. Zhang, and H. Zeng, “Robust ferromagnetism in Mn-doped MoS₂ nanostructures,” *Appl. Phys. Lett.* **109**, 092401 (2016).
- ⁸K. Zhang, S. Feng, J. Wang, A. Azcatl, N. Lu, R. Addou, N. Wang, C. Zhou, J. Lerach, V. Bojan, *et al.*, “Manganese doping of monolayer MoS₂: the substrate is critical,” *Nano Lett.* **15**, 6586–6591 (2015).
- ⁹Y. Miao, Y. Huang, H. Bao, K. Xu, F. Ma, and P. K. Chu, “Tunable magnetic coupling in Mn-doped monolayer MoS₂ under lattice strain,” *J. Phys. Condens. Matter* **30**, 215801 (2018).
- ¹⁰H. Tan, W. Hu, C. Wang, C. Ma, H. Duan, W. Yan, L. Cai, P. Guo, Z. Sun, Q. Liu, *et al.*, “Intrinsic ferromagnetism in Mn-Substituted MoS₂ nanosheets achieved by supercritical hydrothermal reaction,” *Small* **13**, 1701389 (2017).

- ¹¹V. Kuraganti, A. Jain, R. Bar-Ziv, A. Ramasubramaniam, and M. Bar-Sadan, “Manganese Doping of MoSe₂ Promotes Active Defect Sites for Hydrogen Evolution,” *ACS Appl. Mater. Interfaces* **11**, 25155–25162 (2019).
- ¹²S. H. Lee, Y. Zhu, Y. Wang, L. Miao, T. Pillsbury, H. Yi, S. Kempinger, J. Hu, C. A. Heikes, P. Quarterman, W. Ratcliff, J. A. Borchers, H. Zhang, X. Ke, D. Graf, N. Alem, C.-Z. Chang, N. Samarth, and Z. Mao, “Spin scattering and noncollinear spin structure-induced intrinsic anomalous Hall effect in antiferromagnetic topological insulator MnBi₂Te₄,” *Phys. Rev. Research* **1**, 012011 (2019).
- ¹³M. Wang, D. Williams, G. Lahti, S. Teshima, D. D. Aguilar, R. Perry, and K. J. Koski, “Chemical intercalation of heavy metal, semimetal, and semiconductor atoms into 2D layered chalcogenides,” *2D Mater.* **5**, 045005 (2018).
- ¹⁴M. Whittingham, “Lithium and sodium intercalated dichalcogenides: Properties and electrode applications,” *Prog. Solid State Chem.* **12**, 41 (1978).
- ¹⁵M. S. Dresselhaus, *Intercalation in layered materials*, Vol. 148 (Springer, 2013).
- ¹⁶W. Müller-Warmuth and R. Schöllhorn, *Progress in intercalation research*, Vol. 17 (Springer Science & Business Media, 2012).
- ¹⁷K. P. Chen, F. R. Chung, M. Wang, and K. J. Koski, “Dual element intercalation into 2D layered Bi₂Se₃ nanoribbons,” *J. Am. Chem. Soc.* **137**, 5431–5437 (2015).
- ¹⁸A. Sood, F. Xiong, S. Chen, H. Wang, D. Selli, J. Zhang, C. J. McClellan, J. Sun, D. Donadio, Y. Cui, E. Pop, and K. E. Goodson, “An electrochemical thermal transistor,” *Nat. Commun.* **9**, 4510 (2018).
- ¹⁹S. Chen, A. Sood, E. Pop, K. E. Goodson, and D. Donadio, “Strongly tunable anisotropic thermal transport in MoS₂ by strain and lithium intercalation: first-principles calculations,” *2D Mater.* **6**, 025033 (2019).
- ²⁰F. Gamble, F. DiSalvo, R. Klemm, and T. Geballe, “Superconductivity in layered structure organometallic crystals,” *Science* **168**, 568–570 (1970).
- ²¹M. Wang, I. Al-Dhahir, J. Appiah, and K. J. Koski, “Deintercalation of zero-valent metals from two-dimensional layered chalcogenides,” *Chem. Mater.* **29**, 1650–1655 (2017).
- ²²W. Bao, J. Wan, X. Han, X. Cai, H. Zhu, D. Kim, D. Ma, Y. Xu, J. N. Munday, H. D. Drew, *et al.*, “Approaching the limits of transparency and conductivity in graphitic materials through lithium intercalation,” *Nat. Commun.* **5**, 4224 (2014).
- ²³Y. Gong, H. Yuan, C.-L. Wu, P. Tang, S.-Z. Yang, A. Yang, G. Li, B. Liu, J. van de Groep,

- M. L. Brongersma, *et al.*, “Spatially controlled doping of two-dimensional SnS₂ through intercalation for electronics,” *Nat. Nano.* **13**, 294 (2018).
- ²⁴G. Zhu, J. Liu, Q. Zheng, R. Zhang, D. Li, D. Banerjee, and D. G. Cahill, “Tuning thermal conductivity in molybdenum disulfide by electrochemical intercalation,” *Nat. Commun.* **7**, 13211 (2016).
- ²⁵M. Wang and K. J. Koski, “Reversible chemochromic MoO₃ nanoribbons through zerovalent metal intercalation,” *ACS Nano* **9**, 3226–3233 (2015).
- ²⁶G. Froehlicher, E. Lorchat, O. Zill, M. Romeo, and S. Berciaud, “Rigid-layer raman-active modes in n-layer transition metal dichalcogenides: interlayer force constants and hyperspectral raman imaging,” *J. Raman. Spectrosc.* **49**, 91–99 (2018).
- ²⁷K. F. Mak, C. Lee, J. Hone, J. Shan, and T. F. Heinz, “Atomically thin MoS₂: a new direct-gap semiconductor,” *Phys. Rev. Lett.* **105**, 136805 (2010).
- ²⁸Q. H. Wang, K. Kalantar-Zadeh, A. Kis, J. N. Coleman, and M. S. Strano, “Electronics and optoelectronics of two-dimensional transition metal dichalcogenides,” *Nat. Nanotech.* **7**, 699 (2012).
- ²⁹M. Ersfeld, F. Volmer, P. M. M. C. de Melo, R. de Winter, M. Heithoff, Z. Zanolli, C. Stampfer, M. J. Verstraete, and B. Beschoten, “Spin states protected from intrinsic electron–phonon coupling reaching 100 ns lifetime at room temperature in MoSe₂,” *Nano Letters* **19**, 4083–4090 (2019).
- ³⁰S. Caramazza, F. Capitani, C. Marini, A. Mancini, L. Malavasi, P. Dore, and P. Postorino, “Effect of pressure on optical properties of the transition metal dichalcogenide MoSe₂,” in *J. Phys. Conf. Ser.*, Vol. 950 (IOP Publishing, 2017) p. 042012.
- ³¹L. Yang, L. Dai, H. Li, H. Hu, K. Liu, C. Pu, M. Hong, and P. Liu, “Pressure-induced metallization in MoSe₂ under different pressure conditions,” *RSC Advances* **9**, 5794–5803 (2019).
- ³²Z. Zhao, H. Zhang, H. Yuan, S. Wang, Y. Lin, Q. Zeng, G. Xu, Z. Liu, G. Solanki, K. Patel, *et al.*, “Pressure induced metallization with absence of structural transition in layered molybdenum diselenide,” *Nat Commun.* **6**, 7312 (2015).
- ³³V. L. Johnson, A. Anilao, and K. J. Koski, “Pressure-dependent phase transition of 2D layered silicon telluride (Si₂Te₃) and manganese intercalated silicon telluride,” *Nano Res.* **12**, 2373–2377 (2019).
- ³⁴N. Wahlberg, N. Bindzus, L. Bjerg, J. Becker, A.-C. Dippel, and B. B. Iversen, “Syn-

- chrotron powder diffraction of silicon: high-quality structure factors and electron density,” *Acta Crystallogr. A* **72**, 28–35 (2016).
- ³⁵J. P. Perdew and A. Zunger, “Self-interaction correction to density-functional approximations for many-electron systems,” *Phys. Rev. B* **23**, 5048 (1981).
- ³⁶P. Giannozzi, O. Andreussi, T. Brumme, O. Bunau, M. B. Nardelli, M. Calandra, R. Car, C. Cavazzoni, D. Ceresoli, M. Cococcioni, *et al.*, “Advanced capabilities for materials modelling with Quantum ESPRESSO,” *J. Phys. Condens. Matter* **29**, 465901 (2017).
- ³⁷P. E. Blöchl, “Projector augmented-wave method,” *Phys. Rev. B* **50**, 17953 (1994).
- ³⁸G. Kresse and D. Joubert, “From ultrasoft pseudopotentials to the projector augmented-wave method,” *Phys. Rev. B* **59**, 1758 (1999).
- ³⁹V. I. Anisimov, J. Zaanen, and O. K. Andersen, “Band theory and Mott insulators: Hubbard U instead of Stoner I,” *Phys. Rev. B* **44**, 943–954 (1991).
- ⁴⁰M. Cococcioni and S. de Gironcoli, “Linear response approach to the calculation of the effective interaction parameters in the LDA+U method,” *Phys. Rev. B* **71**, 035105 (2005).
- ⁴¹F. Zhou, M. Cococcioni, C. A. Marianetti, D. Morgan, and G. Ceder, “First-principles prediction of redox potentials in transition-metal compounds with LDA+U,” *Phys. Rev. B* **70**, 235121 (2004).
- ⁴²L. Wang, T. Maxisch, and G. Ceder, “Oxidation energies of transition metal oxides within the GGA+U framework,” *Phys. Rev. B* **73**, 195107 (2006).
- ⁴³A. Jain, G. Hautier, S. P. Ong, C. J. Moore, C. C. Fischer, K. A. Persson, and G. Ceder, “Formation enthalpies by mixing GGA and GGA+U calculations,” *Phys. Rev. B* **84**, 045115 (2011).
- ⁴⁴A. N. Andriotis and M. Menon, “Tunable magnetic properties of transition metal doped MoS₂,” *Phys. Rev. B* **90**, 125304 (2014).
- ⁴⁵M. Wu, X. Yao, Y. Hao, H. Dong, Y. Cheng, H. Liu, F. Lu, W. Wang, K. Cho, and W.-H. Wang, “Electronic structures, magnetic properties and band alignments of 3d transition metal atoms doped monolayer MoS₂,” *Phys. Lett. A* **382**, 111–115 (2018).
- ⁴⁶S. Baroni, S. de Gironcoli, A. Dal Corso, and P. Giannozzi, “Phonons and related crystal properties from density-functional perturbation theory,” *Rev. Mod. Phys.* **73**, 515–562 (2001).
- ⁴⁷C. Rice, R. J. Young, R. Zan, U. Bangert, D. Wolverson, T. Georgiou, R. Jalil, and K. S. Novoselov, “Raman-scattering measurements and first-principles calculations of strain-

- induced phonon shifts in monolayer MoS₂,” *Phys. Rev. B* **87**, 081307(R) (2013).
- ⁴⁸F. Wang, I. A. Kinloch, D. Wolverson, R. Tenne, A. Zak, E. O’Connell, U. Bangert, and R. J. Young, “Strain-induced phonon shifts in tungsten disulfide nanoplatelets and nanotubes,” *2D Mater.* **4**, 015007 (2016).
- ⁴⁹D. Wolverson, S. Crampin, A. S. Kazemi, A. Ilie, and S. J. Bending, “Raman Spectra of Monolayer, Few-Layer, and Bulk ReSe₂: An Anisotropic Layered Semiconductor,” *ACS Nano* **8**, 11154–11164 (2014).
- ⁵⁰The 1T phase for MoSe₂ is unstable and intercalated systems relax into a lower-symmetry 1T’ phase with a larger unit cell.
- ⁵¹G. K. Madsen and D. J. Singh, “Boltztrap. a code for calculating band-structure dependent quantities,” *Computer Physics Communications* **175**, 67 – 71 (2006).
- ⁵²D. M. Guzman, N. Onofrio, and A. Strachan, “First principles investigation of copper and silver intercalated molybdenum disulfide,” *J. Appl. Phys.* **121**, 055703 (2017).
- ⁵³The formation energies discussed here are obtained with LSDA+U and are systematically lower than those computed by LSDA, which however exhibit the same trends. Formation energies are summarized in Table S1.
- ⁵⁴G. Eda, H. Yamaguchi, D. Voiry, T. Fujita, M. Chen, and M. Chhowalla, “Photoluminescence from chemically exfoliated mos₂,” *Nano Letters* **11**, 5111–5116 (2011).
- ⁵⁵Y. Cheng, A. Nie, Q. Zhang, L.-Y. Gan, R. Shahbazian-Yassar, and U. Schwingenschlogl, “Origin of the phase transition in lithiated molybdenum disulfide,” *ACS Nano* **8**, 11447–11453 (2014).
- ⁵⁶A. Powell, “Intercalation compounds of low-dimensional transition metal chalcogenides,” *Annu. Rep. Prog. Chem., Sect. C: Phys. Chem.* **90**, 177–213 (1993).
- ⁵⁷O. Agnihotri, H. Sehgal, and A. Garg, “Laser excited raman spectra of Gr. VI semiconducting compounds,” *Solid State Commun.* **12**, 135–138 (1973).
- ⁵⁸D. Nam, J.-U. Lee, and H. Cheong, “Excitation energy dependent raman spectrum of MoSe₂,” *Sci. Rep.* **5**, 17113 (2015).
- ⁵⁹P. D. Lao, Y. Guo, G. G. Siu, and S. C. Shen, “Optical-phonon behavior in Zn_{1-x}Mn_xSe: Zinc-blende and wurtzite structures,” *Phys. Rev. B* **48**, 11701 (1993).
- ⁶⁰N. Onofrio, D. Guzman, and A. Strachan, “Novel doping alternatives for single-layer transition metal dichalcogenides,” *J. Appl. Phys.* **122**, 185102 (2017).
- ⁶¹J. Karthikeyan, H.-P. Komsa, M. Batzill, and A. V. Krasheninnikov, “Which transition

metal atoms can be embedded into two-dimensional molybdenum dichalcogenides and add magnetism?” *Nano Letters* **19**, 4581–4587 (2019).

⁶²B. W. Reed, D. R. Williams, B. P. Moser, and K. J. Koski, “Chemically tuning quantized acoustic phonons in 2D layered MoO₃ nanoribbons,” *Nano letters* **19**, 4406–4412 (2019).

⁶³T. Sekine, M. Izumi, T. Nakashizu, K. Uchinokura, and E. Matsuura, “Raman scattering and infrared reflectance in 2H-MoSe₂,” *J. Phys. Soc. Jpn.* **49**, 1069–1077 (1980).

⁶⁴R. Aksoy, E. Selvi, and Y. Ma, “X-ray diffraction study of molybdenum diselenide to 35.9 GPa,” *J. Phys. Chem. Solids* **69**, 2138–2140 (2008).